Mona Taghavikish, Surya Subianto, Naba Kumar Dutta, Liliana de Campo, Jitendra P. Mata, Christine Rehm, and Namita Roy Choudhury

Polymeric ionic liquid nanoparticle emulsions as a corrosion inhibitor in anticorrosion coatings

ACS Omega, 2016; 1(1):29-40

Published version http://dx.doi.org/10.1021/acsomega.6b00027

ACS OMEGA

Article

http://pubs.acs.org/journal/acsodf

Polymeric Ionic Liquid Nanoparticle Emulsions as a Corrosion Inhibitor in Anticorrosion Coatings

Mona Taghavikish,[†] Surya Subianto,[†] Naba Kumar Dutta,[†,‡] Liliana de Campo,[§] Jitendra P. Mata,[§] Christine Rehm,[§] and Namita Roy Choudhury*[,†,‡]

[†]Future Industries Institute, Mawson Lakes Campus, University of South Australia, Mawson Lakes, Adelaide, SA 5095, Australia

[‡]School of Chemical Engineering, University of Adelaide, Adelaide, SA 5005, Australia

[§]Bragg Institute, ANSTO, New Illawarra Rd, Lucas Heights, Sydney, NSW 2234, Australia

Supporting Information

ABSTRACT: In this contribution, we report the facile preparation of cross-linked polymerizable ionic liquid (PIL)-based nanoparticles via thiol−ene photopolymerization in a miniemulsion. The synthesized PIL nanoparticles with a diameter of about 200 nm were fully characterized with regard to their chemical structures, morphologies, and properties using different techniques, such as Fourier transform infrared spectroscopy, thermogravimetric analysis, scanning electron microscopy, and transmission electron microscopy. To gain an in-depth understanding of the physical and morphological structures of the PIL nanoparticles in an emulsion, small-angle neutron scattering and ultra-small-angle neutron scattering were used. Neutron scattering studies revealed valuable information regarding the formation of cylindrical ionic micelles in the spherical nanoparticles, which is a unique property of this system. Furthermore, the PIL nanoparticle emulsion was utilized as an inhibitor in a self-assembled nanophase particle (SNAP) coating. The corrosion protection ability of the resultant coating was examined using potentiodynamic polarization and electrochemical impedance spectroscopy. The results show that the PIL nanoparticle emulsion in the SNAP coating acts as an inhibitor of corrosion and is promising for fabricating advanced coatings with improved barrier function and corrosion protection.

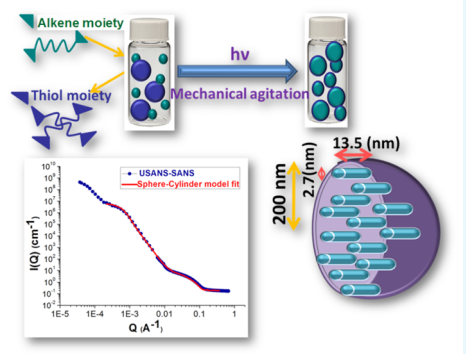

INTRODUCTION

Recently, polymerizable ionic liquid (PIL)-based nanoparticles have received significant interest as a new class of functional polymers that combines both the properties of ionic liquids (ILs) with polyelectrolyte characteristics and improved mechanical durability and dimensional control. Polymer nanoparticles have been conveniently prepared either from preformed polymers, by methods including precipitation, solvent evaporation, dialysis, and supercritical fluid expansion, or by direct polymerization of monomers using classical polymerization, including microemulsion, miniemulsion, surfactant-free emulsion, and interfacial polymerization.[1] The preparation of PILs as nanoparticles via suspension polymerization,[2] water-in-oil concentrated emulsion polymerization,[3] and precipitation polymerization in water without stabilizers using IL monomers with long alkyl chains has been recently reported.[4,5] Because of their dense charge and IL functionality, PIL nanoparticles have an important role in the practical design of various functional materials, such as catalyst supports, binders, coatings, and sensors.[6] One example of this type of application is work by Yang et al.,[7] who reported the preparation of cross-linked PIL microspheres with a diameter of about 200 nm synthesized via miniemulsion polymerization for use as a potential scaffold to immobilize metal nanoparticles for electrocatalysis and heterogeneous catalysis.

Miniemulsion, with droplet sizes typically in the range of 20−200 nm, is one of the most common methods used for the fabrication of polymer nanoparticles in a water-borne system. The use of water as the dispersion medium is one of the main advantages of this system, which makes it environmentally friendly and also allows it to have excellent heat dissipation during the polymerization process.[8]

Recently, "click" polyaddition reactions in miniemulsions, specifically thiol-mediated chemistry (i.e., thiol−ene/yne, thiol-Michael), have attracted attention as facile methods for the synthesis of polymer microparticle, nanoparticle, and nanocapsule dispersions in heterophase media with high efficiency.[9−11] The earliest example of using a thiol−ene reaction in a miniemulsion system was reported by Van Berkel et al.[12] This involved thiol−ene chemistry for the facile surface functionalization of composite nanoparticles dispersed in a wide variety of solvents. On the other hand, a recent example of the incorporation of thiol−ene chemistry into a water-borne

Received: April 26, 2016
Accepted: June 15, 2016
Published: July 6, 2016

DOI: 10.1021/acsomega.6b00027
ACS Omega 2016, 1, 29−40

Scheme 1. General Reaction Scheme for the Development of Water-Borne Thiol−Ene Polymer Nanoparticles

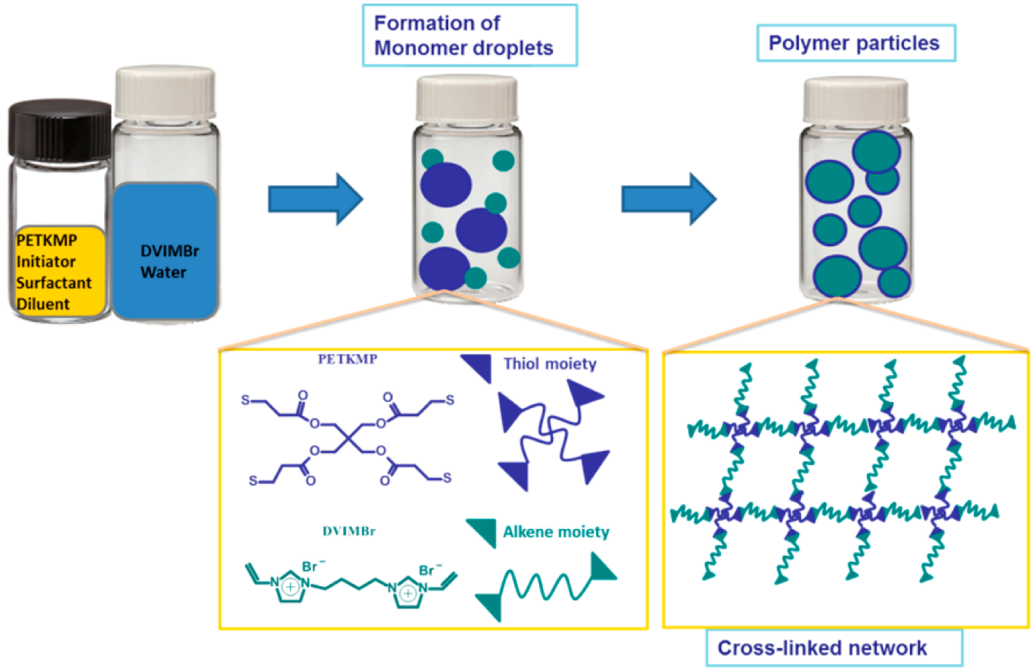

system by Shipp and co-workers reported water-borne thiol−ene photopolymerization that yields dispersions of polymer particles.[13] In another work by the same group, the effect of surfactants on particle size and stability was investigated, where they found that during water-borne thiol−ene photopolymerization the use of emulsifying agents is crucial to prevent particle aggregation.[14] Similarly, Amato et al. reported the synthesis of small, sub-100 nm cross-linked polythioether nanoparticles using miniemulsion thiol−ene photopolymerization.[8] The authors studied the effects of the miniemulsion formulation, including inhibitors, surfactant concentration, and monomer weight fraction as well as process parameters such as ultrasonication time and amplitude, on nanoparticle size.

Considering the synergistic properties of PILs and thiol−ene photopolymerization, combining the two certainly broadens their application potential.[15] Because there are relatively few examples of the combination of thiol-mediated polyadditions in dispersed systems with PILs, there is a significant opportunity to exploit thiol-mediated polyadditions in miniemulsions using PILs for the fabrication of cross-linked functional polymer nanoparticles. In our previous work, we reported the facile preparation of polymerizable IL-based gel beads using thiol−ene click chemistry and illustrated their unique properties as multipurpose materials suitable for pH sensing or anticorrosion applications.[16]

Since ILs are known to inhibit corrosion in metals, the PIL emulsion system is expected to exhibit corrosion inhibition properties when incorporated into inorganic sol−gel coatings, such as a self-assembled nanophase particle (SNAP) coating. Unlike free ILs, they would be immobilized within the coating and thus should provide better protection against the leaching of free ILs from the SNAP coating, which has shown good anticorrosion properties on materials such as aluminum alloys.[17] However, its potential for metals has not been fully explored with respect to low carbon steel. Unlike polymer-based paints, inorganic coatings are prone to crack formation and hence become more permeable, but their ability to bond with surface oxides and hydroxides makes them promising materials for use as interfacial layers.

In this article, we demonstrate the fabrication of cross-linked PIL-based nanoparticles via thiol−ene photopolymerization in a miniemulsion. By combining thiol−ene and PIL functionalities in a water-based system, we demonstrate the application of these nanoparticles in anticorrosion coatings. This is the first report on the application of PIL-based nanoparticles in anticorrosion coatings, where the particles were characterized for their structure, size, shape, electrochemical performance, using neutron scattering, microscopy, and electrochemical techniques.

EXPERIMENTAL SECTION

Materials. Pentaerythritol tetrakis(3-mercaptopropionate) (PETKMP), 1-vinylimidazole, 1,4-dibromobutane, benzophenone (BP), Triton X-100, azobis(isobutyronitrile) (AIBN), sodium dodecyl sulfate (SDS), (3-aminopropyl)triethoxysilane, sorbitan monostearate, toluene, acetone, hexane diethyl ether, and methanol (analytical grade) were obtained from Sigma-Aldrich and used without further purification. Fluorosurfactant FC-4432 was obtained from 3M. Double distilled water (DDW) was used for all experiments.

Synthesis of 1,4-Di(vinylimidazolium)butane Bisbromide. 1,4-Di(vinylimidazolium)butane bisbromide (DVIMBr) was synthesized by stirring a 2:1 molar ratio mixture of 1-vinylimidazole and 1,4-dibromobutane in methanol at 60 °C for 15 h. Upon cooling, the reaction mixture was poured dropwise into 1 L of diethyl ether. The white precipitate was filtered off and dried at room temperature until the weight was constant, with a yield of 68%.[4]

^{1}H NMR (300 MHz, D_2O, δ, ppm): 8.98 (2H), 7.69 (2H), 7.49 (2H), 7.04 (2H), 5.75 (2H), 5.33 (2H), 4.21 (4H), 1.87 (4H).

Miniemulsion Thiol−Ene Photopolymerization. A typical miniemulsion photopolymerization reaction for the synthesis of PIL nanoparticle involves the mixing of two

DOI: 10.1021/acsomega.6b00027
ACS Omega 2016, 1, 29−40

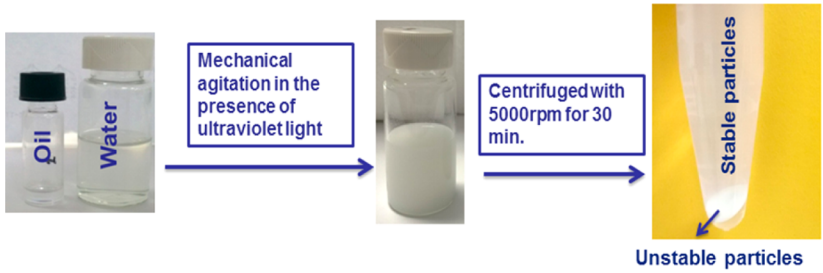

Figure 1. Fabrication of PIL nanoparticles through thiol−ene photopolymerization.

separate phases, an organic phase and an aqueous phase. The organic phase consists of 0.24 g of PETKMP dissolved in 0.1 mL of toluene and mixed with 0.1 g of Triton surfactant (2.5 wt % with respect to the monomer) and 18.2 mg of benzophenone (BP) photoinitiator (5 wt % with respect to the monomer concentration). Separately, an aqueous phase was prepared by dissolving 0.4 g of DVIMBr in 9 mL of DDW. The organic phase was added to the aqueous solution dropwise using a syringe needle, and the reaction mixture was stirred for approximately 5−10 min and then ultrasonicated in an ice bath for 10 min at an amplitude of 50% to emulsify the organic phase in the aqueous phase and to create nanodroplets. Finally, photopolymerization was performed in the presence of ultraviolet light (365 nm wavelength) inside a black box for another 1 h with continuous stirring, resulting in cross-linked polymer nanospheres and a stable emulsion (Scheme 1). The solution was degassed before and after photopolymerization to remove any bubbles.

The emulsion solution was centrifuged at 5000 rpm for 30 min at room temperature. As a result, two fully separated phases formed: one phase containing unstable particles and unreacted monomers and another phase with stable PIL particles that was collected in the water phase (Figure 1). PIL nanoparticles were washed with methanol and toluene to remove any trace of impurities. The concentration of PIL nanoparticles before centrifugation was 35 mg/mL, which was decreased to 23 mg/mL after removing all of the unreacted monomer. Collecting PIL nanoparticles in the water phase has the advantage that characterization is easier.

Preparation of the PIL Nanoparticle-Based Coating. Coatings were prepared using SNAP as a matrix for coating and for the addition of different concentrations of the emulsion to improve the barrier and protective properties of the SNAP coating. The SNAP coating was prepared by the method proposed by Donley et al.[17] Mild steel substrates (CA3SN-G, 0.08% carbon contents, thickness ∼ 0.6 mm, 1.7 cm × 1.7 cm) were cleaned using a process reported by our group.[18] The coating solutions with a total volume of 20 mL were prepared by diluting 7 mL of SNAP solution with DDW by a factor of 1.75. In order to find an optimized concentration of the PIL nanoparticle emulsion, three different concentrations (0.4, 0.8, and 1.6 wt %) of the emulsion were added to the SNAP solution followed by the addition of surfactant (3M FC-4432, 0.04 % w/v). Then, the mixtures were ultrasonicated at 50% for 5 min to obtain homogeneous solutions. At the end, (3-aminopropyl)triethoxysilane cross-linking agent was added into the solutions, and the final mixture was vigorously stirred and applied to cleaned metal substrates by dip coating at a withdrawal speed of 10 cm/min. The coated sample was dried at room temperature for 24 h to allow solvent evaporation. Finally, the coating was thermally cured at 80 °C and 60% humidity overnight in a humidity oven (ESPEC model SH-241).

Characterization. ^{1}H NMR analysis was performed on a 300 MHz Bruker Avance spectrometer at room temperature using deuterium oxide (D_2O) as the solvent. Infrared spectra of the gels were acquired using a Nicolet Magna-IR spectrometer 750 in photoacoustic mode with 256 scans and a carbon black reference.

Quantitative analysis of particle size was done via dynamic light scattering (DLS) using a Nano ZS Zetasizer (Malvern Instruments Ltd.) equipped with a 633 nm He−Ne laser to measure the hydrodynamic size distribution of the PIL nanoparticles in aqueous solutions. Differential scanning calorimetry (DSC) measurements were conducted using a TA Instruments Discovery DSC. The instrument was calibrated to obtain the baseline and cell constant prior to running the experiments. The samples were sealed in hermetic aluminum pans for use in the DSC experiment, and an empty pan was used as the reference. The temperature range for the experiment was from −70 to 200 °C, with a heating rate of 10 °C/min, under a controlled nitrogen gas flow of 50 mL/min. Thermogravimetric analysis (TGA) was performed using a TA Instruments Discovery TGA with an aluminum pan. The samples were subjected to a 10 °C/min ramp rate from 100 to 550 °C under a nitrogen atmosphere. The size and morphology of the particles were analyzed by optical microscopy (Prism optical microscope) and field emission scanning electron microscopy (FE-SEM) using a Philips XL30 FEG instrument operated at an acceleration voltage of 15 kV. For electron microscopy analysis, the sample was placed on indium tin oxide (ITO)-coated glass as a conducting surface, and images were taken without any further coating. In addition, morphologies of the coatings surface were observed using SEM, where compositions were analyzed from the energy dispersive spectroscopy (EDS) module (OXFORD instruments) attached to the microscope.

Also, a JEOL 2100F transmission electron microscope (TEM) was used for size characterization, which was operated at 200 kV with a resolution ∼2 Å.

Small-angle neutron scattering (SANS) experiments were performed with a QUOKKA SANS instrument at OPAL, Australian Nuclear Science and Technology Organization (ANSTO),[19] with a neutron beam from a large liquid-D_2 cold source (5 Å) using sample-to-2D detector distances of 2, 8, and 20 m. The sample concentration was 0.8 wt % and was run using Helma quartz cells (2 mm path length in D_2O). The measurements and analyses were conducted at 25 °C using a scattering vector, Q, ranging from 6.9×10^{-4} to 0.5 Å^{-1}. The D_2O background was subtracted from the sample.

Ultra-small-angle neutron scattering (USANS) experiments were carried out with the KOOKABURRA instrument at

DOI: 10.1021/acsomega.6b00027
ACS Omega 2016, 1, 29−40

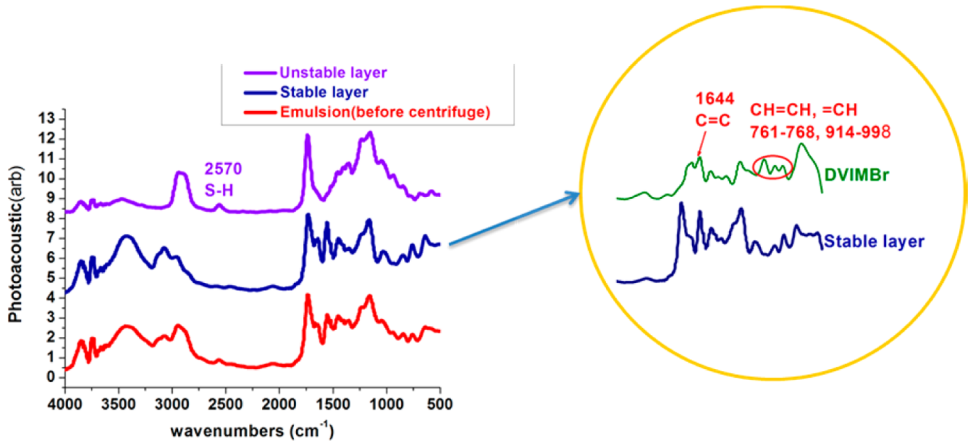

Figure 2. FTIR spectra of emulsions before and after centrifugation and comparison with spectra of a stable layer with DVIMBr.

OPAL (ANSTO, Lucas Heights, Sydney) using a long wavelength, 4.74 Å. The measurements were conducted at room temperature. The USANS data were reduced using an empty sample container as background and converted to absolute scale using python scripts based on the standard procedure.[20] The Q range covered using USANS was 2.9×10^{-5} to 1.8×10^{-2} Å^{-1}. The experimental data were desmeared using the Lake algorithm, incorporated in the NIST USANS macros,[20] before they were merged with the SANS data. The structural parameters of the nanoparticle emulsion were obtained from fits of the SANS and USANS data using the SasView program.

Utilizing a technique based on the Wilhelmy balance principle, advancing and receding contact angles were measured using a dynamic contact angle analyzer at a constant velocity (100 μm/s) and 23 °C (42% relative humidity in a clean room). The advancing and receding contact angles were determined using the scanning Wilhelmy plate method for the SNAP, emulsion, and SNAP/0.8 wt % emulsion (optimized concentration). The substrates used for these contact angle investigations were clean steel metal plates with 12.7 mm length and 0.12 mm thickness. The plates were cleaned with acetone and ethanol and dried with a nitrogen flow before each experiment. The surface tension of the coatings was also measured by the Wilhelmy plate using a platinum plate with 19.9 mm length and 0.2 mm thickness. The advancing and receding contact angles were calculated from the scanning Wilhelmy plate result.

Electrochemical characterization of the uncoated and coated samples was carried out using a standard corrosion cell (1 L, Pine Research Instrumentation) with a conventional three electrode setup in a nondeaerated 3.5 wt % NaCl solution prepared from analytical grade chemicals (ChemSupply, Australia) and distilled water (Milli-Q). A saturated calomel electrode (SCE, Pine Research Instrumentation, +0.24 V vs normal hydrogen electrode, NHE) was employed as the reference electrode, a graphite rod of 2 mm diameter was used as the counter electrode, and the sample under test served as the working electrode. All reported potentials in this article (determined using electrochemical techniques) are with reference to the SCE. Initially, the open circuit potential (OCP) of the specimens was determined as a function of time, and the samples were allowed to stabilize at their OCP for 1 h before measurements. Potentiodynamic polarization analysis was conducted at a scan rate of 1 mV/s in the potential range of ±300 mV relative to OCP. Electrochemical impedance spectroscopy (EIS) measurements were performed using a Solartron 1260 impedance/gain-phase analyzer in combination with a Solartron 1280B electrochemical interface. The impedance measurements were carried out in a 1 MHz to 10 kHz frequency range with 40 steps per decade. All spectra were recorded at OCP with an applied 10 mV sinusoidal perturbation. The impedance data was fitted using Zview software and a model for permeable coating consisting of resistive elements (due to solution resitance R_s, coating resistance R_{coat}, and interfacial resistance R_{int}) and constant phase elements (to represent imperfect capacitors due to coating capacitance CPE_{coat} and interfacial capacitance CPE_{int}), where the parameters obtained from the constant phase elements are used to calculate the capacitance using the relationship $C = R^{([1-n]/n)} \times Q^{(1/n)}$, where R is the resistance parallel to the constant phase elements, Q is the pseudo capacitance, and n is the phase change value obtained from fitting.

RESULTS AND DISCUSSION

PIL Nanoparticles by Miniemulsion Photopolymerization. PIL-based nanoparticles were synthesized via thiol−ene photopolymerization in a miniemulsion. The thiol−ene miniemulsion was prepared using an organic phase of PETKMP, a photoinitiator, Triton, and solvent, which was then added to an aqueous phase consisting of water and DVIMBr. A stoichiometric ratio of precursors PETKMP to DVIMBr was chosen. A water-immiscible solvent such as toluene was used to facilitate emulsification as well as to lower the viscosity of the dispersed phase. Once it was mixed, the organic phase was then emulsified in the aqueous phase via ultrasonication to create PIL nanoparticles (1:10 oil-to-water ratio). Centrifugation has been used as a means to isolate PIL nanoparticles. The use of a centrifuge to separate microcapsules is reported in the literature by Szabó et al.[21]

The stability and size of polymer nanoparticles obtained from heterogeneous miniemulsion photopolymerization are strongly influenced by several process parameters, including surfactant structure and initiators. To examine this effect on the stability of the emulsion, the effects of different surfactants and initiators have been studied. When the thermal initiator (AIBN) was replaced with BP, this resulted in colloidally unstable latexes and significant coagulum formation. However, the same system in bulk form has been prepared using either thermal or

DOI: 10.1021/acsomega.6b00027
ACS Omega 2016, 1, 29−40

photoinitiator polymerization, and the behavior of the synthesized polymer is similar.[16] Additionally, two reaction systems, each with a different surfactant, were examined in order to obtain the most stable emulsion. In one system, anionic surfactant SDS was used in the water phase, and in the other system, nonionic surfactant sorbitan was replaced with Triton. In the presence of an anionic surfactant, we observed phase separation and settling of the PIL nanoparticles to the bottom of the aqueous phase. When attractive forces between surfactant molecules and particles are dominant, the particles will adhere; however, if the repulsive forces are stronger, then the particles will remain suspended separately.[22] In this system, the attractive van der Waals interactions between the Br^- group in PIL and Na^+ in SDS lead to phase separation.[23] In contrast, when using a nonionic surfactant like sorbitan, the surfactant layer provides steric stabilization to keep the nanoparticles from aggregating. However, a weak adsorption of the surfactant on the particles (in the case of sorbitan) resulted in the coalescence of emulsion droplets after a couple of hours.

With Triton, long-term stability of the emulsion system can be achieved due to the fact that nonionic surfactants (such as Triton X-100) do not ionize in aqueous solution because their hydrophilic groups are nondissociable.[24] Therefore, there will be no ions to interact with Br^- in the IL and destabilize the system. Thus, Triton was chosen for the rest of the studies presented here.

Structure and Morphology of PIL Nanoparticles. To investigate the chemical composition of the emulsion and characteristics of each layer after centrifugation, FTIR analysis of the sample before and after centrifugation was performed, and the spectra are presented in Figure 2. As discussed earlier, after centrifugation, the solution was separated into two layers. As can be seen in Figure 1, before centrifugation the emulsion is a white, milky color, which separates into a clear stable top layer and an unstable white bottom layer after centrifugation. In the stable top layer, the FTIR spectrum does not show any band due to sulfur−hydrogen stretching around 2570 cm^{-1}, and there is an absence of the C═C vinyl peak at 1644 cm^{-1}. This observation confirms that the thiol and vinyl groups have fully reacted in this layer. Furthermore, a comparison of the spectrum of the unstable layer with PETKMP also confirms that the bottom layer contains unreacted thiol groups. However, in both layers, there was a reduction in the intensity of the peaks due to vinyl groups at 3080 cm^{-1} and around the 761−768 and 914−998 cm^{-1} regions (in comparison with the DVIMBr spectra), which confirms the consumption of vinyl groups in both layers. Since it appears that the main difference between the two layers is unreacted thiol groups, these results suggest that fully cured, stoichiometric particles are well-dispersed and stable in the stable layer (unaffected by centrifugation) due to the hydrophilicity of the PIL, whereas any unreacted reagents and those with a nonstoichiometric (less than 1:2 DVIMBr/PETKMP) composition formed unstable aggregates that settle to the bottom layer after centrifugation because of the more hydrophobic nature of the thiol component (PETKMP).

Analysis of the PIL particle size was performed using an optical microscope, SEM, and DLS (Figure 3). For optical microscopy, samples were prepared by air-drying or drying in a vacuum oven on glass slides, whereas for SEM, due to the need for a conductive substrate for improved resolution, the emulsion was dried on ITO glass. DLS results of the particle dispersion in water showed a hydrodynamic particles size

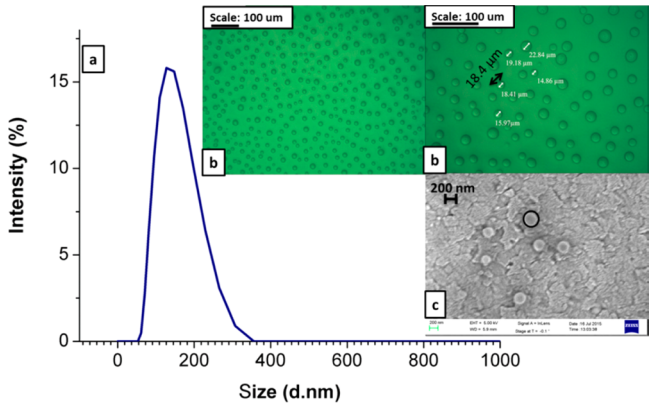

Figure 3. (a) Size distribution of PIL nanoparticles in dilute solutions as determined by DLS, (b) microscopy images of dried PIL nanoparticles on glass slides, and (c) SEM image of dried PIL nanoparticles on ITO-coated glass.

(diameter) around 200 nm, which is in very good agreement with SEM results (Figure 3c); however, the optical images of dried samples show a larger particle size of around 20 μm (Figure 3b). This is attributed to the difference in the substrates used for optical and SEM microscopies, that is, by drying the sample for the optical image some of the particles aggregate and become larger, as illustrated in Figure 3b. Interestingly, although the same aggregation phenomenon is seen in some part of the ITO glass (as seen in the SEM images), this is significantly reduced. This may be due to the comparatively rough nature of the ITO surface "trapping" some of the individual emulsion particles and thus preventing them from coalescing to form larger aggregates as the solvent dries.

Considering the significant role that surfactants play in particle size and stabilization, we investigated the effect of surfactant concentration on particle formation. In this investigation, emulsions were made with varying Triton surfactant concentrations of 0.2, 0.4, and 0.8 wt %. DLS and TEM were used to compare the results of this study, and the results are shown in Figure S1. As can be seen from the TEM images, at the lowest surfactant concentration (Figure S1a), the particles are small and spherical, but there appears to be a greater variation in particle size. DLS analysis also indicates a dual distribution centered at around 150 and 700 nm, which indicates aggregation of the particles in solution due to the low surfactant concentration. Larger particles were not observed in the TEM images. Increasing the surfactant concentration to 0.4 wt % (Figure S1b) results in particles that are similar in size but with a narrower distribution. DLS analyses of the particles show a single distribution with a particle size of around 200 nm, which corresponds well with the microscopy results. Further increasing the surfactant concentration to 0.8 wt % resulted in much broader particle size distributions and larger particles (as observed in TEM images, Figure S1c), which may be due to excess surfactant material affecting particle formation. This is because an excess of surfactant may lead to an attraction between multiple particles in solution, causing the polymer particles to undergo destabilization and aggregation. Thus, the surfactant concentration of 0.4 wt % was considered to be optimal and was used for all investigations.

USANS/SANS of the Nanoparticle Emulsion. Detailed SANS and USANS studies were undertaken to characterize the microstructure (USANS) and nanostructure (SANS) of the emulsion, as well as to obtain a better understanding of the

DOI: 10.1021/acsomega.6b00027
ACS Omega 2016, 1, 29−40

shape, size, and internal structure of the PIL nanoparticles. Figure 4 shows the combined SANS/USANS data for the

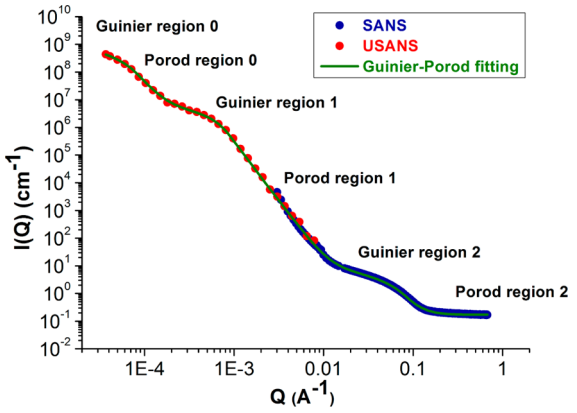

Figure 4. Combined USANS and SANS curves for the nanoparticle emulsion with combined Guinier–Porod fitting.

nanostructured emulsion, where the extended Q range provides an extraordinary opportunity to study its hierarchical structure. USANS data, covering the range of 3.5×10^{-5} to 1×10^{-2} Å^{-1}, provide information on the microscale, which covers the particle size and interparticle distances, whereas SANS data in the Q range above 1×10^{-2} provide information on the internal structure of the gel nanoparticles. A sufficient overlap within the USANS and SANS data was taken to ensure a good fit when the two data sets were combined.

The combined view of the SANS/USANS data in Figure 4 shows three shoulders: the first two are attributed to the particle sizes at low Q, and the third is attributed to the internal structures in the emulsion in the higher Q range. Distinct Guinier and Porod regions are visible for the three shoulders. The three distinct regions are fitted with three combined Guinier–Porod models, which can be used to fit scattering data from both spherical and non spherical objects[25] using SASView. This gives the radius of gyration (R_g) of the scattering objects, Porod exponent values, and the dimensional variable(s), which are summarized in Table 1. The scattering at the very low Q region points towards a small amount of very large particles that will be excluded from further analysis. The parameters obtained from the Guinier–Porod fit provide useful information for further modeling of the USANS and SANS data.

Table 1. Summary of R_g, Porod Exponents, and Dimensional Variable of Nanoparticle Emulsion Obtained from Guinier–Porod Fitting of USANS and SANS Data

Q region (from Figure 4)	R_g (Å)	m (Porod exponent)	S (dimensional variable)
very low Q (USANS) region 0	23530 (±740)	3.6 ((±0.03))	0.6 ((±0.06))
low Q (USANS) region 1	2916.0 (±0.2)	4.31 (±0.01)	0 (±0.05)
high Q (SANS) region 2	20.1 (±0.6)	3.93 (±0.02)	0.79 (±0.02)

For the USANS region, we know from the other techniques that the scattering comes from polydisperse spherical emulsion droplets. The Porod exponent of 4 in this region (Porod region 1) represents a smooth surface of the scattering particles. A dimensionality of 0 is expected for objects with a known spherical shape.[25,26] A R_g of 291 nm is larger than the radius we obtained from DLS and microscopy, which indicated a particle size of around 150–200 nm (diameter). This can be attributed to the difference in concentration as well as the impact of the average particle size. Indeed, USANS measures an intensity average, so large particles are much more visible and will be weighted more than small particles. Thus, the average size will be larger than for the other averages.

Concerning the internal emulsion structure, determined in the SANS region, the Porod exponent (Porod region 2) was also close to 4, indicative of a smooth surface of the scattering objects. The obtained dimensionality value close to 1 points toward cylindrical structures, which is also suggested by a clear porod slope of Q^{-1} in Guinier region 2 (Figure 4).

On the basis of the Guinier–Porod model analysis, a sphere model was used to model the scattering profile of the PIL nanoparticle emulsion, which is consistent with the expected shape of the nanoparticles based on other data such as microscopy. The scattering length density (SLD) of the D_2O solvent and the nanoparticles was kept fixed at 5.76×10^{-6} and 4.48×10^{-6}, respectively, during data fitting because they were determined on the basis of the material properties and were not expected to vary significantly from bulk materials.

In the SANS region, the slope of −1 in Guinier region 1, as well as the dimensional variable from the Guinier–Porod model, suggests a cylindrical shape of the particles in the higher Q region; thus, a cylinder model was employed to fit this region. The cylinder model results in a good fit of the data and provides valuable insights into the underlying structure, which could not be detected using other characterization methods due to their lack of contrast (Figure 5a). Unlike other methods, the SANS contrast comes from the presence of D_2O in the ionic domains; thus, SANS scattering is expected to arise due to internal structures within the gel particles where the ionic PIL domains would be swollen with D_2O. Fitting with the cylinder model gives a length of ∼13.5 nm and a radius of 2.7 nm (27 Å).

On the basis of these values, obtained from fitting neutron scattering data and other known data for the material, it is evident that the PIL nanoparticle emulsion is composed of spheres of around 200 nm in size, the internal structure of which consists of cylindrical domains with a size of roughly 2.7 nm, which could not be detected using a non-neutron-based technique due to a lack of contrast (Figure 5b). Therefore, neutron scattering provides valuable insight and an in-depth understanding of particle formation and its arrangements in an emulsion system.

Phase Behavior of PIL Nanoparticles. In order to investigate the phase behavior and glass transition temperature (T_g) of the PIL nanoparticle emulsion, different thermal techniques were employed. DSC analysis of a dried nanoparticle emulsion sample revealed a T_g of −53 °C for PIL nanoparticles obtained using the miniemulsion method (Figure 6a), whereas in our previous study, the bulk PIL gel obtained using a solvent evaporation method showed a T_g of −23 °C (Figure 6b),[16] indicating that the composition and network structure of the polymer produced in the water-borne system were more elastic than those obtained using the more traditional solvent evaporation system. The DSC results also show that the glass-to-rubber transition occurs over a relatively narrow temperature range, indicating a homogeneous network structure, which is typical of thiol–ene polymers.

TGA analysis of both the stable dispersion and the nonstoichiometric precipitate layer after centrifugation showed

DOI: 10.1021/acsomega.6b00027
ACS Omega 2016, 1, 29–40

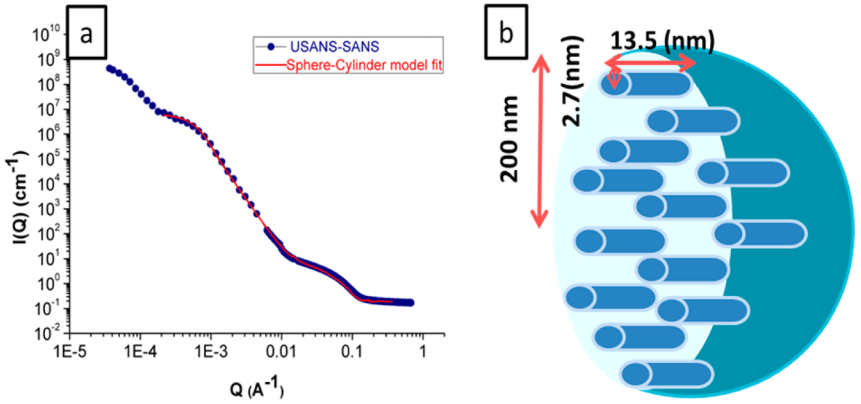

Figure 5. (a) Scattering data and sphere and cylinder model fit to USANS−SANS data. (b) Proposed structure of the PIL nanoparticle emulsion based on neutron scattering data.

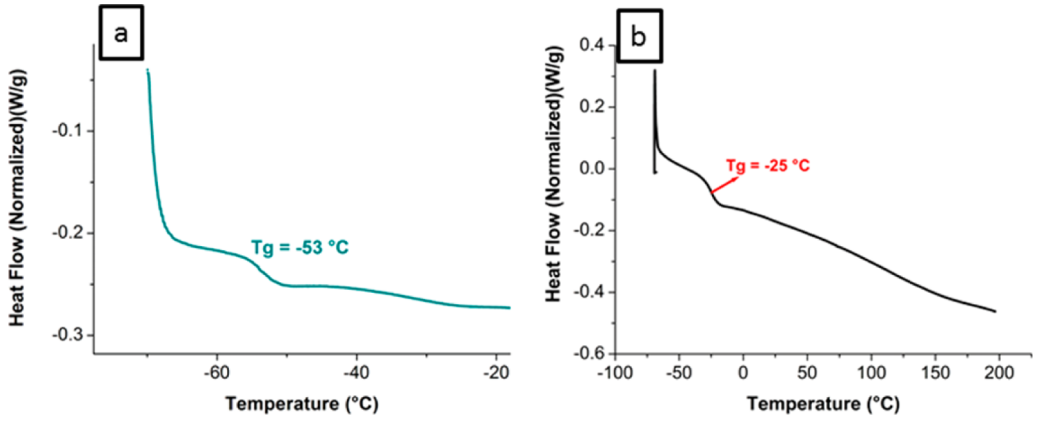

Figure 6. DSC thermogram showing the glass transition temperature of (a) PIL nanoparticles and (b) PIL gel beads under a temperature ramp of 10 °C/min.

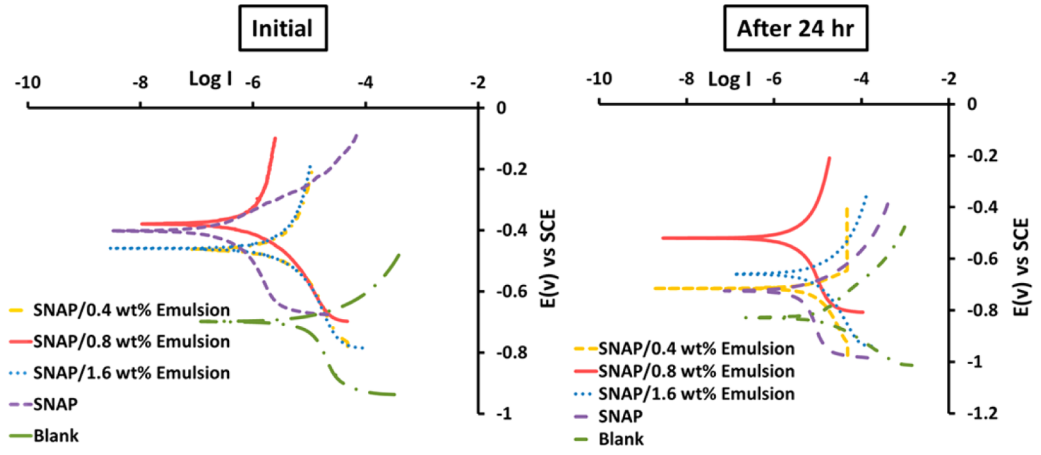

Figure 7. Potentiodynamic analysis of SNAP PIL emulsion coated samples at three different emulsion concentrations, blank metal, and the SNAP coating alone at the beginning of the experiment and after 24 h of immersion in a 3.5 wt % NaCl solution.

that the well-dispersed PIL nanoparticles in the top layer were thermally stable up to 305 °C under nitrogen, which was similar to that of bulk PIL gel (Figure S2). However, the precipitate showed two degradation temperatures around 350 and 450 °C, which correlate to free IL and some unreacted thiols, which indicates that unreacted thiols and vinyl monomers were not stable in the dispersion and thus were selectively removed by centrifugation.

Additionally, the phase behavior of the SNAP/emulsion coating was investigated using TGA and DSC. TGA analysis of SNAP (Figure S3a) has only one degradation temperature around 430 °C, which was altered to two temperatures (400 and 500 °C) in the SNAP with PIL nanoparticles. This could be attributed to a structural change of the emulsion due to the addition of SNAP, which was also proved with DSC results. DSC of both the SNAP and SNAP/emulsion samples did not show any T_g, which is due to the inorganic SNAP coating

DOI: 10.1021/acsomega.6b00027
ACS Omega 2016, 1, 29−40

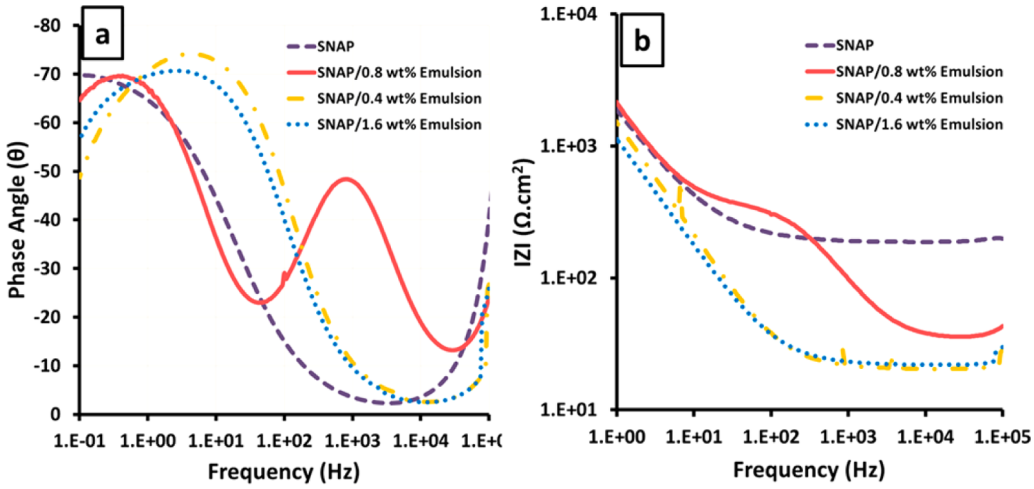

Figure 8. (a) Phase angle and (b) Bode plot as a function of frequency for SNAP with emulsion coated samples at three different concentrations in comparison with those of SNAP alone.

(which is inorganic and thus shows no glass transition) being the major component. Additionally, since PIL emulsion nanoparticles were present only in small quantities (0.8 wt %), their T_g was not detected in the DSC analysis (Figure 3Sb).

Evaluation of Corrosion Resistance. *Potentiodynamic Polarization.* To evaluate and understand the corrosion protection mechanism of the PIL-emulsion-loaded SNAP coating (which will be referred to here as SNAP/emulsion for simplicity), potentiodynamic polarization measurements were carried out. The PIL loading for this study was initially chosen based on previous results using microcontainers such as halloysite.[27] To find the optimum concentration of the PIL nanoparticle emulsion to use for achieving a better efficiency on an interfacial layer of the coating, a potentiodynamic polarization study of SNAP, SNAP with three different concentrations of the emulsions (PIL nanoparticles) (0.4, 0.8, and 1.6 wt %), and blank metal was carried out, and the results are shown in Figure 7 for the coated samples for both the initial samples and after 24 h of measurement in aqueous salt solution (3.5 wt % NaCl). The corrosion current density (I_{corr}) and corrosion potential (E_{corr}) values were then estimated by fitting the anodic and cathodic polarization curves using CORRVIEW software, and the values are presented in Table S1.

Initially, the I_{corr} value of the SNAP/0.8 wt % emulsion coated samples was lower by 2 orders of magnitude in comparison with that of blank metal and is very close to the I_{corr} for the SNAP-coated sample, as would be expected for a barrier coating. However, after 24 h, there was an order of magnitude increase in I_{corr} for pristine SNAP compared to that of the SNAP/0.8 wt % emulsion coated sample. On the other hand, the SNAP coatings containing 0.4 and 1.6 wt % emulsions showed higher I_{corr} compared to that of pristine SNAP. After 24 h of immersion in salt solution, all of the emulsion-containing samples showed a significantly lower increase in I_{corr} compared to that of pristine SNAP, with the best-performing system being the SNAP/0.8 wt % emulsion sample. This can be attributed to the presence of the optimum concentration of PIL nanoparticles, which reinforce the SNAP structure and prevent it from corroding. When a lower or higher concentration of the emulsion was used, I_{corr} increased compared to that of SNAP, which indicates that at these concentrations the emulsion particles are not acting synergistically, interfering with and weakening the efficiency of the SNAP coating. Therefore, the better protection of the SNAP/0.8 wt % emulsion could be attributed to the fact that this amount of emulsion has better miscibility with the SNAP structure, enhancing the performance of the SNAP coating and providing better protection of the metal surface. Moreover, the inhibition efficiency E_I (%) is calculated from values of I_{corr} using the following equation[28]

$$E_I\ (\%) = \frac{I_{corr} - I'_{corr}}{I_{corr}} \times 100 \quad (1)$$

where I_{corr} and I'_{corr} are uninhibited and inhibited corrosion current densities, respectively. These results are also indicative of the SNAP/0.8 wt % emulsion having a better E_I, with the highest value of 78.6% (Table S1).

The SNAP/0.8 wt % emulsion also shows the best corrosion protection based on the E_{corr} values, showing a more noble E_{corr} (−0.3769 V) among the samples and remaining at more noble potentials (−0.5192) after 24 h. The shifting of the E_{corr} values to the noble potential indicates enhanced corrosion resistance due to the inhibition effect of the coatings. In the case of the 0.4 and 1.6 wt % samples, the E_{corr} is shifted to more negative values, as it can be seen that the final E_{corr} values are very similar to those of pristine SNAP, indicating that these concentrations are not structurally optimal.

It has been reported that imidazolium compounds show corrosion-resistant behavior on steel due to the specific interaction between the −C═N− group and electronegative nitrogen in the molecule with the metal surface.[29] Therefore, such an interaction is highly likely in the present system and can also result in the observed reduction in the changes in E_{corr} of SNAP/emulsion in comparison to pristine SNAP due to the use of imidazolium-based IL emulsion particles in this formulation.

EIS Investigation. EIS was used to investigate the nature of the coatings. Figure 8 shows the Bode plot of the impedance modulus vs frequency and phase angle vs frequency for the coated samples. The impedance modulii for the SNAP and SNAP/emulsion coated samples at three different concentrations decrease in the following order: |Z| (SNAP/0.8 wt % emulsion) > |Z| (SNAP) > |Z| (SNAP/1.6 wt % emulsion) > |Z| (SNAP/0.4 wt % emulsion). This is in agreement with the inhibiting efficiency demonstrated by the Tafel plot in Figure 7, where the SNAP/0.8 wt % emulsion coated sample shows the

DOI: 10.1021/acsomega.6b00027
ACS Omega 2016, 1, 29−40

lowest I_{corr}, which correlates to a higher impedance for this type of coating.

As illustrated in Figure 8a, the SNAP and SNAP/emulsion coated samples exhibit similar profiles except for the SNAP/0.8 wt % emulsion coated sample, which exhibits an additional time constant at middle frequencies. The first time constant at low frequency observed in all samples is commonly associated with the diffusion of electrolyte and corrosion activity on the substrate surface. However, the presence of another time constant at middle frequencies in the impedance spectrum of the SNAP/0.8 wt % emulsion indicates the presence of another interface due to an intermediate layer formed by the interaction of the emulsion with the metal surface, which could be due to the presence of the imidazolium groups on the PIL. Such behavior (an increase in the phase angle at middle frequencies) can be indicative of the presence of ionic species at the metal−coating interface.[30] In this case, since the EIS measurements were done after only a short equilibration (and thus this increase in the phase angle is unlikely to be due to corrosion), this extra time constant can be attributed to an emulsion interface between the SNAP coating and the metal surface, which indicates the preferential migration of the emulsion particles at the metal surface during the dip-coating process, as confirmed with a wettability study.

In order to better understand this phenomenon, an electrical equivalent circuit was used to analyze and model the impedance data. In general, semipermeable coatings can be modeled by the equivalent circuit displayed in Figure 9, which takes into account the resistance of the solution, coating, and interface, with capacitive elements due to the bulk coating and the metal/coating interface.[30,31] The impedance spectra of SNAP and SNAP/0.8 wt % emulsion samples were fitted using this model.

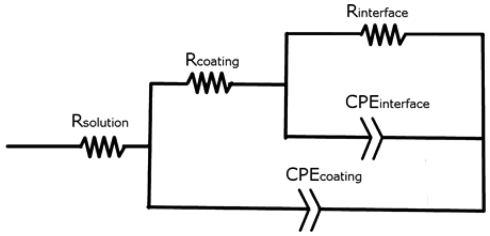

Figure 9. Electrical equivalent circuit used to model the impedance data of a permeable coating.

Modeling of the impedance results as shown on the Nyquist plot in Figure 10a shows that the coating resistance increases but the interfacial resistance decreases for the SNAP/emulsion sample compared to those of pristine SNAP, with the coating resistance increasing from 180 to 348 Ω and the interfacial resistance decreasing from 578 to 61 kΩ (Table 2). The presence of the emulsion particles in the SNAP coating also increases the coating capacitance and the interfacial capacitance, which could be due to the ionic nature of these emulsion particles, resulting in a greater amount of charges in both the bulk coating and at the metal−coating interface.

Table 2. Values Obtained from Fitting the Impedance Data

sample	$R_{solution}$ (Ω)	$R_{coating}$ (Ω)	$C_{coating}$ (F)	$R_{interface}$ (Ω)	$C_{interface}$ (F)
SNAP only	7	180	6.71×10^{-9}	578 320	5.31×10^{-4}
SNAP only 24 h	8	156	7.98×10^{-9}	1305	2.01×10^{-3}
SNAP/ emulsion	33	348	2.24×10^{-6}	61 499	1.26×10^{-4}
SNAP/ emulsion 24 h	22	365	2.15×10^{-6}	8925	2.40×10^{-4}

After 24 h, clear differences can be observed in the behavior of the samples with and without the PIL emulsion. In the SNAP-only sample, the initial coating has a very high interfacial resistance, which decreases significantly after 24 h, from 578 to 1.3 kΩ. This reduction of the interfacial resistance is accompanied by an increase in the interfacial capacitance from 0.5 to 2 mF, indicating corrosion on the SNAP−metal interface and potential delamination or blister formation. The coating resistance and capacitance, meanwhile, remain quite similar; thus, this change in the properties of the interface indicates that the SNAP coating, being an interfacial layer rather than a barrier layer, was still permeable to electrolyte, which allows corrosion to occur at the SNAP−metal interface.

Similar to the SNAP samples, the SNAP/emulsion sample after 24 h also shows a significant reduction in interfacial resistance from 61 to 8 kΩ, but this is accompanied by only a slight increase in the interfacial capacitance from 0.12 to 0.24 mF (the coating resistance and capacitance remain relatively unchanged), indicating a similar corrosion process as that of the SNAP sample. However, the interfacial resistance remains higher than that of SNAP alone (8 kΩ for SNAP/emulsion

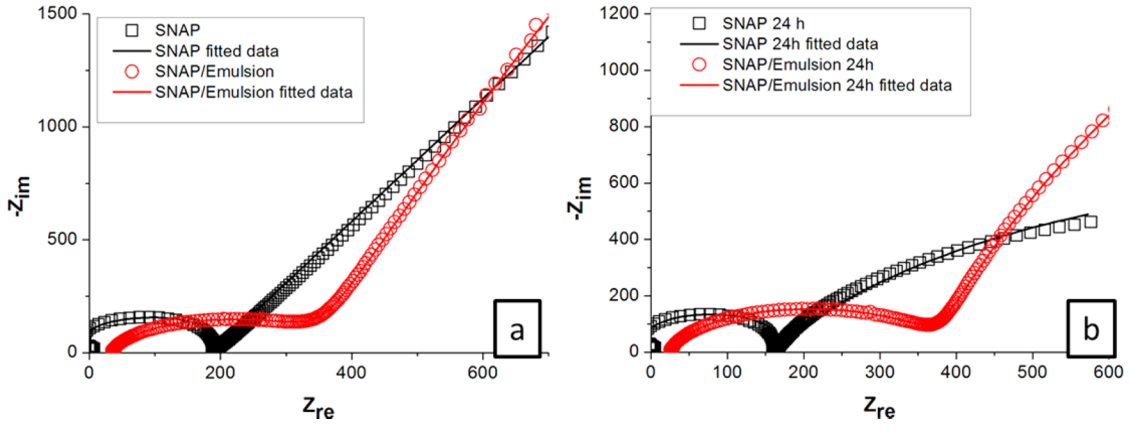

Figure 10. Nyquist plot and fitting results for the SNAP and SNAP/0.8 wt % emulsion coated samples in 3.5% NaCl solution. Impedance measurement was done after (a) 1 h of equilibration and (b) 24 h of immersion.

DOI: 10.1021/acsomega.6b00027
ACS Omega 2016, 1, 29−40

compared to 1.3 kΩ for SNAP alone), which indicates that the presence of the emulsion helps to protect the interface.

The results show that the PIL emulsion slightly increased the resistance of the coating, which indicates that the PIL emulsion resulted in some improvement in the barrier properties of the SNAP coating. Furthermore, some of the emulsion particles may be present at the SNAP−metal interface due to the emulsion particles acting like a surfactant that adheres to the metal surface during coating, resulting in an interfacial layer that contributes to the anticorrosion properties of the coating.

Surface Characterization. Figure 11 shows the SEM surface morphology of blank metal, SNAP, and SNAP/emulsion before and after 1 day of immersion in a 3.5 wt % NaCl solution. Before immersion, the SNAP and SNAP/emulsion coated samples show very smooth, homogeneous surfaces, with some visible particles in the SNAP/emulsion coating. After 24 h of immersion in the salt solution, the image of the blank metal surface (Figure 11a′) shows that it is strongly corroded, resulting in a porous, rough, and heterogeneous surface with visible corrosion products. The SNAP and SNAP/emulsion coated samples (Figure 11b′,c′) also show a roughening of their surface after immersion in the salt solution, with the coating showing a rougher surface after immersion. However, it is evident that the SNAP/emulsion coated sample has retained a smoother and more uniform surface than the SNAP-only sample, which indicates the beneficial effect of the PIL emulsion on the integrity of the SNAP coating.

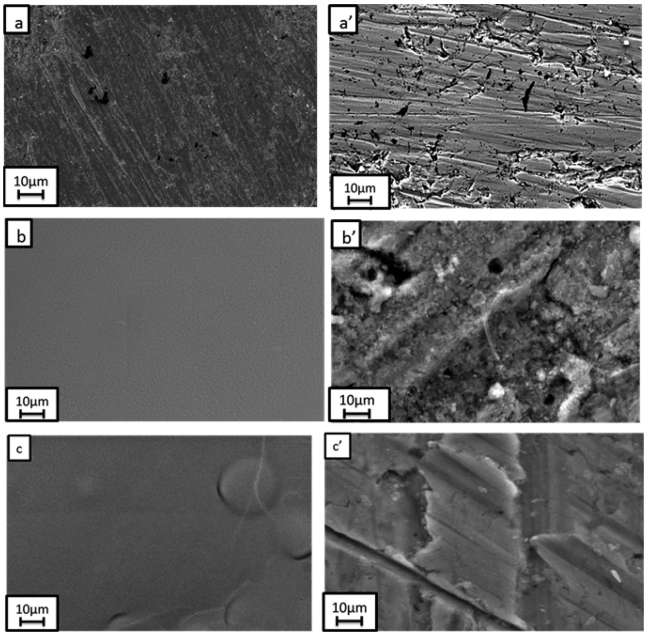

Figure 11. SEM images of (a) and (a′) blank metal, (b) and (b′) SNAP, and (c) and (c′) SNAP/emulsion before and after 24 h in a salt solution, respectively.

EDS data of the surface of the blank metal, SNAP, and SNAP/emulsion coated samples are summarized in Table 3. EDS analysis of the surface of the blank metal (Figure 9b) mostly shows the presence of peaks attributed to Fe and C, specific elements of the steel. After immersing in salt solution (Figure S3), the blank metal surface, which contains mainly Fe and C (with small quantities of Si contaminants), now also shows the presence of oxygen, which indicates the corrosion of iron through the formation of iron oxides. On the other hand,

Table 3. EDS Surface Analysis before and after Immersion in a 3.5 wt % Salt Solution for 24 h

	elemental content (atom %)			
samples	C	O	Fe	Si
blank metal	39.5	0.00	59.4	1.1
blank metal 24 h	38.6	17.5	42.5	1.3
SNAP	56.7	31.8	0.3	11.1
SNAP 24 h	34.4	6.4	58.2	0.9
SNAP/emulsion	57.4	30.7	0.3	11.5
SNAP/emulsion 24 h	34.0	5.1	59.5	1.4

EDS of the surface of the SNAP and SNAP/emulsion coatings were initially showing only carbon, oxygen, and silicon due to the SNAP coating (the oxygen is due to Si−O in the SNAP composition). The appearance of a low oxygen content with a large amount of iron after immersion in the salt solution in the EDS profile of the SNAP and SNAP/emulsion coatings indicates that the SNAP coating may adsorb ferric and ferrous ions; however, the low oxygen content indicates that these species are present as ions and not as oxides. The lower Si content of the coating after immersion supports this as this indicates the presence of ferrous ions that are adsorbed on the surface, and the presence of surface ions would mask the Si from the SNAP coating underneath the adsorbed ions. This result indicates that the SNAP coating strongly binds to ionic species, which may inhibit corrosion through blocking the formation of oxides and scavenging released ions.

Wettability of the Coated Substrate Using the Wilhelmy Balance Technique. To support our hypothesis from the electrochemical analysis results, such as potentiodynamic polarization studies and EIS investigations, which revealed that the PIL nanoparticle emulsion migrates to the interface during the dip-coating process and leads to a better protection mechanism for the SNAP coating, a dynamic wettability study with contact angle measurements was undertaken using the Wilhelmy technique at 23 °C.

A wetting cycle with the SNAP system is shown in Figure S5. In a typical dynamic contact angle measurement, the sample moves against the liquid when the sample is immersed in the liquid and the advancing contact angle is recorded. When the sample emerges, the receding contact angle is measured. It comprises forced and spontaneous movement regions. At the metal−coating interface, the SNAP solution wets the surface well, with the force decreasing marginally. Contact angle hysteresis is also recorded as the difference between the advancing and receding contact angles.[32]

The contact angle data is used to evaluate the dynamic wetting behavior and interaction of the PIL emulsion with the metal surface. Generally, a lower contact angle corresponds to a higher adhesion per unit area, and wetting of the surface is very favorable; thus, the fluid will spread over a large area of the surface. The work of adhesion was also calculated from the contact angle as follows

$$\omega_a = \Upsilon_l(1 + \cos\theta) \quad (2)$$

where Y_1 is the surface tension of the liquid and θ is the contact angle.[33] Table 4 shows the physical properties, such as viscosity and surface tension, of the probe liquids as well as the work of adhesion and contact angle.

It is interesting to note that the viscosity of the emulsion (1 mPas) is one-half of that of the SNAP solution, and the surface tension is also the lowest compared to all samples. One of the

DOI: 10.1021/acsomega.6b00027
ACS Omega 2016, 1, 29−40

Table 4. Physical Properties of the Probe Liquids and Wettability of the Metal with SNAP, Emulsion, and SNAP/0.8 wt % Emulsion

sample	viscosity (mPas)	surface tension (mN/m)	advancing contact angle (deg)	work of adhesion (mN/m)
SNAP	2.1	37.6	65.2 ± 2	53.4
0.8 wt % emulsion	1.0	31.9	52.4 ± 1.6	51.4
SNAP/0.8 wt % emulsion	1.9	37.5	52.3 ± 1.9	60.4

important criteria of good adhesion is that the coating should wet the surface.[34,35] Therefore, the surface energy of the substrate has to be higher than that of the organic coating, which is in agreement with the data obtained in this study. The surface tension of all coatings is far below the surface tension value for steel, which ranges from 700 to 1100 mN/m depending on the cleaning process.[36] The results indicate that the lower the angle, the higher the surface polarity, resulting in a better work of adhesion.

Moreover, the contact angle value of the emulsion containing sample is in the range of ∼52.4°, indicating that the emulsion samples used in this study wet the surface very well compared to that of stand-alone SNAP (Table 4). This could be attributed to the fact that applying an emulsion to SNAP increases the interaction with the metal surface with high wettability. The contact angle data of the PIL nanoparticle emulsion (surface tension 31.9 vs 37.5 mN/m) compared to that of the SNAP nanoparticle solution indicates a strong affinity and preferential diffusion and adsorption of the PIL nanoparticle emulsion onto the metal surface. As a result, it could act as inhibitor layer with improved barrier performance against the diffusion of oxygen and moisture into the metal surface by the adsorbed layer. Figure S6 illustrates the diffusion pathway into the metal surface using SNAP and SNAP with emulsion coating. The strong affinity of the PIL nanoparticle emulsion to the metal substrate leads to a stronger interfacial layer at the interface, which illustrates its potential to be used as an organic inhibitor in SNAP or other coatings.

CONCLUSIONS

We report the facile preparation of cross-linked PIL-based nanoparticles via thiol−ene photopolymerization in miniemulsions. The utilization of this method offers great potential for the development of cross-linked polymer nanoparticles in the water phase. The synthesized PIL nanoparticles were fully characterized for their chemical structures, morphologies, and properties. SAS analysis provided valuable insight into the physical and molecular arrangements of the nanoparticles in the emulsion. Furthermore, in this study, we applied PIL nanoparticles at different concentrations into a SNAP-based interfacial layer on mild steel surfaces. Potentiodynamic polarization and EIS investigations show that the sample containing 0.8 wt % of the emulsion improved the inhibitor properties of the coating. EIS and contact angle/wettability studies also revealed that these nanoparticles improve the corrosion resistance of the SNAP−metal interface by preferentially migrating to the metal surface during coating because there is a strong affinity between the PIL nanoparticle emulsion and the metal surface. This shows the potential for these PIL nanoparticle emulsions to enhance the corrosion protection ability of SNAP-based coatings.

ASSOCIATED CONTENT

Supporting Information

The Supporting Information is available free of charge on the ACS Publications website at DOI: 10.1021/acsomega.6b00027.

TEM images of emulsion particles at different concentrations, DLS data, TGA data, and a summary table of potentiodynamic polarization and wettability studies (PDF)

AUTHOR INFORMATION

Corresponding Author

*E-mail: namita.choudhury@unisa.edu.au; namita.roychoudhury@adelaide.edu.au. Tel.: +6188302 3719.

Notes

The authors declare no competing financial interest.

ACKNOWLEDGMENTS

The authors gratefully acknowledge the financial support of the Australian Research Council's Linkage grant for carrying out this work and also the industry partner Wave Rider Energy. Access to the SANS (QUOKKA) and USANS (KOOKABURRA) facility at ANSTO, Lucas Heights, Sydney, was supported through an ANSTO beam time award (proposal 4492).

REFERENCES

(1) Rao, J. P.; Geckeler, K. E. Polymer nanoparticles: Preparation techniques and size-control parameters. *Prog. Polym. Sci.* **2011**, *36*, 887−913.

(2) Muldoon, M. J.; Gordon, C. M. Synthesis of gel-type polymer beads from ionic liquid monomers. *J. Polym. Sci., Part A: Polym. Chem.* **2004**, *42*, 3865−3869.

(3) Marcilla, R.; Sanchez-Paniagua, M.; Lopez-Ruiz, B.; Lopez-Cabarcos, E.; Ochoteco, E.; Grande, H.; Mecerreyes, D. Synthesis and characterization of new polymeric ionic liquid microgels. *J. Polym. Sci., Part A: Polym. Chem.* **2006**, *44*, 3958−3965.

(4) Yuan, J.; Antonietti, M. Poly(ionic liquid) Latexes Prepared by Dispersion Polymerization of Ionic Liquid Monomers. *Macromolecules* **2011**, *44*, 744−750.

(5) Yuan, J.; Soll, S.; Drechsler, M.; Müller, A. H. E.; Antonietti, M. Self-Assembly of Poly(ionic liquid)s: Polymerization, Mesostructure Formation, and Directional Alignment in One Step. *J. Am. Chem. Soc.* **2011**, *133*, 17556−17559.

(6) Men, Y.; Kuzmicz, D.; Yuan, J. Poly(ionic liquid) colloidal particles. *Curr. Opin. Colloid Interface Sci.* **2014**, *19*, 76−83.

(7) Yang, J.; Qiu, L.; Liu, B.; Peng, Y.; Yan, F.; Shang, S. Synthesis of polymeric ionic liquid microsphere/Pt nanoparticle hybrids for electrocatalytic oxidation of methanol and catalytic oxidation of benzyl alcohol. *J. Polym. Sci., Part A: Polym. Chem.* **2011**, *49*, 4531−4538.

(8) Amato, D. V.; Amato, D. N.; Flynt, A. S.; Patton, D. L. Functional, sub-100 nm polymer nanoparticles via thiol-ene miniemulsion photopolymerization. *Polym. Chem.* **2015**, *6*, 5625−5632.

(9) Hoyle, C. E.; Lee, T. Y.; Roper, T. Thiol−enes: Chemistry of the past with promise for the future. *J. Polym. Sci., Part A: Polym. Chem.* **2004**, *42*, 5301−5338.

(10) Hoyle, C. E.; Bowman, C. N. Thiol−Ene Click Chemistry. *Angew. Chem., Int. Ed.* **2010**, *49*, 1540−1573.

(11) Hoyle, C. E.; Lowe, A. B.; Bowman, C. N. Thiol-click chemistry: a multifaceted toolbox for small molecule and polymer synthesis. *Chem. Soc. Rev.* **2010**, *39*, 1355−1387.

DOI: 10.1021/acsomega.6b00027
ACS Omega 2016, 1, 29−40

(12) Van Berkel, K. Y.; Hawker, C. J. Tailored composite polymer−metal nanoparticles by miniemulsion polymerization and thiol-ene functionalization. *J. Polym. Sci., Part A: Polym. Chem.* **2010**, *48*, 1594−1606.
(13) Durham, O. Z.; Krishnan, S.; Shipp, D. A. Polymer Microspheres Prepared by Water-Borne Thiol−Ene Suspension Photopolymerization. *ACS Macro Lett.* **2012**, *1*, 1134−1137.
(14) Durham, O. Z.; Shipp, D. A. Suspension thiol-ene photopolymerization: Effect of stabilizing agents on particle size and stability. *Polymer* **2014**, *55*, 1674−1680.
(15) Wei, H.; Wang, Y.; Guo, J.; Shen, N. Z.; Jiang, D.; Zhang, X.; Yan, X.; Zhu, J.; Wang, Q.; Shao, L.; Lin, H.; Wei, S.; Guo, Z. Advanced micro/nanocapsules for self-healing smart anticorrosion coatings. *J. Mater. Chem. A* **2015**, *3*, 469−480.
(16) Taghavikish, M.; Subianto, S.; Dutta, N. K.; Choudhury, N. R. Facile Fabrication of Polymerizable Ionic Liquid Based-Gel Beads via Thiol−ene Chemistry. *ACS Appl. Mater. Interfaces* **2015**, *7*, 17298−17306.
(17) Donley, M. S.; Mantz, R. A.; Khramov, A. N.; Balbyshev, V. N.; Kasten, L. S.; Gaspar, D. J. The self-assembled nanophase particle (SNAP) process: A nanoscience approach to coatings. *Prog. Org. Coat.* **2003**, *47*, 401−415.
(18) Taghavikish, M.; Subianto, S.; Dutta, N.; Roy Choudhury, N. Novel Thiol-Ene Hybrid Coating for Metal Protection. *Coatings* **2016**, *6*, 17.
(19) Rehm, C.; Brûlé, A.; Freund, A. K.; Kennedy, S. J. Kookaburra: the ultra-small-angle neutron scattering instrument at OPAL. *J. Appl. Crystallogr.* **2013**, *46*, 1699−1704.
(20) Kline, S. Reduction and analysis of SANS and USANS data using IGOR Pro. *J. Appl. Crystallogr.* **2006**, *39*, 895−900.
(21) Szabó, T.; Molnár-Nagy, L.; Bognár, J.; Nyikos, L.; Telegdi, J. Self-healing microcapsules and slow release microspheres in paints. *Prog. Org. Coat.* **2011**, *72*, 52−57.
(22) Diane, J. B., Ed. Physical Stability of Dispersed Systems. In *Injectable Dispersed Systems*; CRC Press, 2005; pp 1−37.
(23) Ahualli, S.; Iglesias, G. R.; Wachter, W.; Dulle, M.; Minami, D.; Glatter, O. Adsorption of Anionic and Cationic Surfactants on Anionic Colloids: Supercharging and Destabilization. *Langmuir* **2011**, *27*, 9182−9192.
(24) Samiey, B.; Cheng, C.-H.; Wu, J. Effects of Surfactants on the Rate of Chemical Reactions. *J. Chem.* **2014**, *2014*, 908476.
(25) Hammouda, B. A new Guinier-Porod model. *J. Appl. Crystallogr.* **2010**, *43*, 716−719.
(26) Krishnamoorti, R.; Silva, A. S.; Modi, M. A.; Hammouda, B. Small-Angle Neutron Scattering Study of a Cylinder-to-Sphere Order−Order Transition in Block Copolymers. *Macromolecules* **2000**, *33*, 3803−3809.
(27) Lvov, Y. M.; Shchukin, D. G.; Möhwald, H.; Price, R. R. Halloysite Clay Nanotubes for Controlled Release of Protective Agents. *ACS Nano* **2008**, *2*, 814−820.
(28) Daoud, D.; Douadi, T.; Issaadi, S.; Chafaa, S. Adsorption and corrosion inhibition of new synthesized thiophene Schiff base on mild steel X52 in HCl and H 2 SO 4 solutions. *Corros. Sci.* **2014**, *79*, 50−58.
(29) Xu, A.; Zhang, F. Z.; Jin, F.; Zhang, R.; Luo, B.; Zhang, T. The Evaluation of Coating Performance by Analyzing the Intersection of Bode Plots. *Int. J. Electrochem. Sci.* **2014**, *9*, 5116−5125.
(30) Wang, H.; Akid, R. A room temperature cured sol−gel anticorrosion pre-treatment for Al 2024-T3 alloys. *Corros. Sci.* **2007**, *49*, 4491−4503.
(31) Banerjee, P.; Woo, R.; Grayson, S.; Majumder, A.; Raman, R. Influence of Zeolite Coating on the Corrosion Resistance of AZ91D Magnesium Alloy. *Materials* **2014**, *7*, 6092.
(32) Gao, L.; McCarthy, T. J. Contact Angle Hysteresis Explained. *Langmuir* **2006**, *22*, 6234−6237.
(33) Ginic-Markovic, M.; Choudhury, N. R.; Dimopoulos, M.; Matisons, J.; Kumudinie, C. Macromolecular modification of EPDM: Wettability, miscibility, and morphology study. *J. Appl. Polym. Sci.* **2001**, *80*, 2647−2661.
(34) Wicks, Z. W.; Jones, F. N.; Pappas, S. P.; Wicks, D. A. Adhesion. In *Organic Coatings*; John Wiley & Sons, Inc., 2006; pp 121−136.
(35) Feldman, D. Fundamentals of adhesion. *J. Polym. Sci., Part A: Polym. Chem.* **1991**, *29*, 1834.
(36) Davim, J. P. *Sustainable Manufacturing*, 1st ed.; John Wiley & Sons, 2013; pp 79−105.

DOI: 10.1021/acsomega.6b00027
ACS Omega 2016, 1, 29−40